energy&fuels

pubs.acs.org/EF
Article

Development of a CFD-DEM Model for a 1 MW_{th} Chemical Looping Gasification Pilot Plant Using Biogenic Residues as Feedstock

Published as part of Energy & Fuels special issue "2024 Pioneers in Energy Research: Juan Adanez".

Christoph Graf,* Florian Coors, Falko Marx, Paul Dieringer, Myrto Zeneli, Panagiotis Stamatopoulos, Konstantinos Atsonios, Falah Alobaid, Jochen Ströhle, and Bernd Epple

Cite This: *Energy Fuels* 2024, 38, 18660−18673

Read Online

ACCESS | Metrics & More | Article Recommendations

ABSTRACT: Chemical looping gasification (CLG) is a novel dual fluidized bed gasification process that enables the conversion of solid feedstocks to a nitrogen-free syngas through in situ air separation, avoiding a costly air separation unit. While there have been recent advances in experimental studies, modeling of CLG is almost exclusively restricted to lab-scale units or 1D models. In this study, a 3D CFD-DEM model of a 1 MW_{th} fuel reactor for the conversion of solid biomass was developed. Due to the high computational demand of the DEM method, a coarse-grained approach was used in combination with a simplified reaction network. The hydrodynamics were modeled with an EMMS drag model. Simulations were conducted for two woody biomasses and wheat straw based on experimental data of a 1 MW_{th} CLG reactor. The model was able to predict the pressure profile over the reactor accurately, with a mean error below 10%. Carbon conversion and oxygen carrier oxidation were in good agreement with the experimental data with mean deviations below 5%, while reasonable values below 8 mol % mean error were achieved for the gas composition. Discrepancies in the gas composition as well as temperature profile indicate that further work is needed in the pyrolysis step of the model.

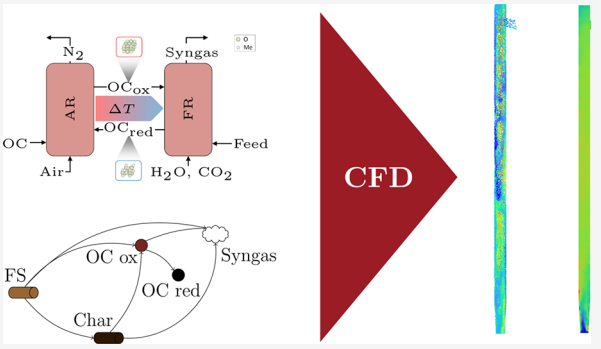

INTRODUCTION

In light of anthropogenic carbon dioxide emissions contributing to climate change, increasing efforts have been made to reduce greenhouse gas emissions and transition the global economy from a fossil-based to a circular system. While carbon emissions have been reduced in the energy and industrial sectors in Europe, emissions are steadily increasing in the transport sector.[1] For land-based transportation, efforts to transition to electric propulsion systems were made; however, this is not feasible for air and sea travel due to the lower energy densities of battery storage compared to liquid fuels. This shows the need for renewable, carbon-neutral liquid fuels.

One possible pathway for the production of such fuels is the gasification of solid biomass residues with subsequent synthesis to products, such as green methanol or Fischer−Tropsch products. Gasification is achieved by partial oxidation of the feedstock to a raw syngas consisting of H_2, CO, CO_2, CH_4, and H_2O along with other trace components, which is subsequently purified for synthesis. To achieve this and avoid dilution of the syngas by nitrogen, pure oxygen is needed as an oxidation agent.[2−4] This is typically provided by an air separation unit, which comes with a large energy demand. The innovative chemical looping gasification (CLG) process functions without pure oxygen.[5]

The CLG process depicted in Figure 1 consists of two reactors, between which an oxygen carrier (OC) is transported. Typically, circulating fluidized bed (CFB) reactors are used due to their high solid transport rates as well as high gas−solid contact intensity. The fuel reactor (FR) acts as the gasifier. The feedstock is converted with gasifying media such as steam or carbon dioxide into syngas. To allow for autothermal operation, oxygen and heat are provided by the OC. The OC enters the reactor in a partially oxidized state at a temperature higher than the FR. Through reaction with syngas components, the OC is reduced, transferring oxygen to the syngas. The reduced OC is transported to the air reactor (AR), where it is reoxidized with air in an exothermal reaction and

Received: May 29, 2024
Revised: August 14, 2024
Accepted: August 30, 2024
Published: September 24, 2024

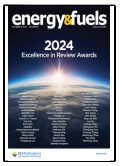

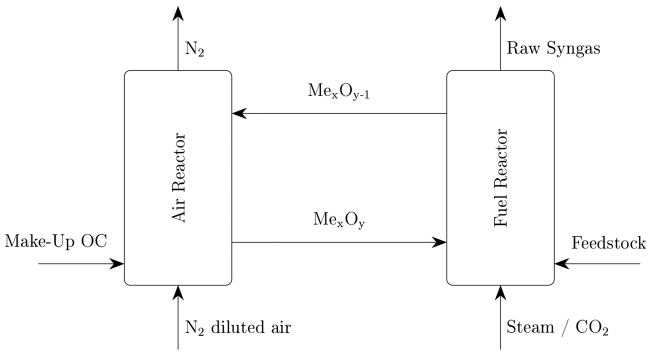

Figure 1. Schematic of the CLG process.

subsequently circulated back to the FR. The air equivalence ratio of the system is controlled through the oxygen content in the AR fluidization, e.g., through mixing air with recycled flue gas.[5]

In recent years, research regarding CLG operation with biomass has been intensified in the experimental field on different scales. Condori et al.[6] investigated biomass CLG using ilmenite as an OC in a 1.5 kW_{th} unit and identified the oxygen-to-biomass ratio as a determining factor for the process efficiency. At 10 kW_{th}, Huseyin et al.[7] used iron- and aluminum-based OC and showed that high efficiency and conversion are possible at sufficiently high temperatures. Ge et al.[8] performed experiments with NiO as an OC in a 25 kW_{th} pilot and showed that the steam-to-biomass ratio has an effect on syngas composition but not on syngas yield. Marx et al.[9] investigated the CLG process at the 1 MW_{th} scale and demonstrated that long-term autothermal operation is possible.

To improve reactor designs and to scale up the CLG process to industrial scales, computational fluid dynamics (CFD) simulation is a powerful and cost-efficient tool. However, only little work has been reported for the CFD simulation of CLG. Some more studies have been performed on chemical looping combustion (CLC). CLC is based on the same process as CLG; however, the oxygen transfer from the AR is increased, aiming at a full feedstock conversion in the FR. Within the CFD framework, different methods are available for modeling the hydrodynamic behavior in fluidized beds. They can be classified as Euler−Euler and Euler−Lagrange approaches as well as hybrid methods.

The Euler−Euler method, often called the two-fluid model (TFM), treats the gas and solid phases as two interpenetrating continuous fluid phases. Effects of particle collisions are accounted for via closure equations based on the kinetic theory of granular flows (KTGF). Using the TFM, Li et al.[10] simulated biomass gasification with hematite as an OC in a lab-scale drop tube reactor. They studied the influence of parameters, such as temperature and steam content, on the gasification products. Du et al.[11] simulated a bench-scale full-loop CFB gasifier operated in batch mode as the FR. They determined suitable operating conditions in a cold flow simulation and extended them to determine the effect of temperature in a reactive simulation. For CLC, several studies have been performed using the TFM. For example, Zhang et al.[12] studied methane combustion at a 200 kW scale using nickel oxide as an OC. They simulated both reactors simultaneously but replaced the coupling elements with time-dependent boundary conditions. Solid fuel gasification with ilmenite was investigated by Mahalatkar et al.[13] at the bench scale. They achieved reasonable predictions of conversion and outlet species distribution for coal. A scale-up to the MW scale was performed by Alobaid et al.,[14] who developed a model based on a quasi-2D fluidized bed and applied this model to a 1 MW_{th} pilot plant. Reasonable results were achieved; however, a dependence on accurate solid circulation measurements was found. May et al.[15] simulated the FR and AR of the same 1 MW_{th} plant and validated their models with experimental data. They achieved a good prediction of the pressure drop in both reactors and carbon slip from the FR to the AR.

The Euler−Lagrange approach treats the particles as discrete spheres that are tracked in the domain through a calculation of the forces acting on the particles. This allows for direct resolution of particle collisions but comes at an increased computational cost. Several methods are available for modeling the collisions. For fluidized beds, the discrete element method (DEM) is suitable, as it enables collisions of multiple particles at the same time. Simulations of CLG or CLC using the DEM are rare due to high computational demand. Yu et al.[16] performed a 2D simulation of a lab-scale bubbling bed reactor for CLG with coal. They found that vertical mixing is dominant compared to horizontal mixing, and overall mixing is improved with higher fluidization velocities. Some models for CLC have been developed. Lin et al.[17] simulated a 0.5 kW coal-fueled FR using ilmenite as an OC. A 2D simulation was performed to save computational time. While some deviations from the experimental results were found, the DEM simulation provided significant improvement compared with the multiphase particle-in-cell (MP-PIC) simulation. A lab-scale 3D reactor with coal and Fe_2O_3 and $MgAl_2O_4$ as an OC was investigated by Banerjee and Agarwal.[18] They showed that the entrainment of particles depended heavily on particle density and that sufficient circulation is difficult to achieve with particles with high particle densities, which are usually required for CLC operation. Methane CLC in a 10 kW unit was simulated by Luo et al.[19] using a Ni-based OC. Pressure distribution was in good agreement with measurement data from cold flow experiments, while the hot solution provided plausible results.

Hybrid approaches combine the advantages of the Euler−Lagrange approach of individual particle tracking such as better representation of particle drag and more natural inclusion of particle size distribution (PSD) with the faster collision treatment of TFM based on KTGF. Within the hybrid regime, a few studies have been published. Dymala et al.[20] simulated biomass CLG at a 1.5 kW scale using the MP-PIC method in Barracuda VR. The plant was operated with ilmenite and milled pine wood. The simulation achieved good agreement with experimental data and could correctly predict trends under different reactor conditions. Further models were developed for CLC by Reinking et al.,[21] who used MP-PIC to predict reactor behavior in a coal-fired 100 kW unit. A full-loop simulation was conducted for 180 s, giving reasonable results but requiring extensive computational time at approximately 1700 h. CLC operation in a 100 kW unit with biomass and a nickel-based OC was simulated by Ahmed and de Lasa[22] using the MP-PIC method. They optimized the solid circulation control between the FR downer and the AR riser.

The DEM approach provides advantages to TFM and hybrid approaches due to resolution of interactions at the particle scale, allowing for accurate modeling of hydrodynamics and particle reactions. This makes DEM a promising tool for CLG

https://doi.org/10.1021/acs.energyfuels.4c02571
Energy Fuels 2024, 38, 18660−18673

simulations if computational limitations can be overcome. Currently, a 3D DEM model for CLG is not available in the literature. In this work, such a model is developed for the FR of a biomass-fired 1 MW_{th} CLG pilot plant. The objectives and novelty of this work are summarized as follows:

1. A comprehensive 3D CFD model using the DEM is provided to accurately describe all relevant processes in the reactor. This model allows for investigations of flow and reaction phenomena to assist in process optimization and reactor scale-up in future works.
2. The model is validated with experimental data of the 1 MW_{th} CLG unit at Darmstadt, Germany, one of the largest CLG units in the world.
3. The model shows the feasibility of the reactive DEM simulation at the MW scale for the CLG process. This model can accurately describe processes on the particle scale allowing for detailed modeling of CLG systems on industrially relevant scales. Due to appropriate simplifications, the simulation can be run within a reasonable time frame.

The paper is structured as follows. First, the CLG process is explained briefly. Second, the mathematical models applied in the model are presented. Then, the experimental and numerical setups are described before the results of the simulations are shown and compared with the experimental data. Finally, a conclusion is drawn regarding the accuracy and applicability of the developed model.

MODELING

1 MW_{th} Pilot Plant. Simulations were conducted for the 1 MW_{th} pilot plant located at Technical University Darmstadt. A detailed description of the plant configuration has been given by Marx et al.,[23] so only the most relevant parts of the simulation are described here. The basic design is shown in Figure 2. The system consists of two CFB reactors connected by two cyclones, two loop seals (LS), and a J-Valve. The FR, which is the focus of this work, has a diameter of 0.4 m and a height of 11.35 m. Solid particles entrained from the FR are separated in the cyclone and transported via a loop seal to the AR. The AR has a diameter of 0.59 m and a height of 8.66 m. Solids exiting the AR are transported via a cyclone to another loop seal. Here, most of the solids flow through the J-Valve to the FR, while the rest is looped back to the AR. The flow through the J-Valve is dependent on its fluidization, thus controlling the global solid circulation.

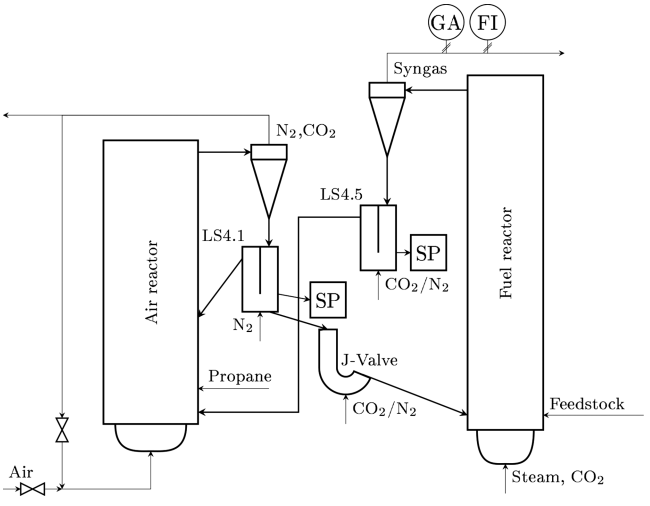

Figure 2. Schematic depiction of the 1 MW_{th} chemical looping pilot plant including relevant measurement equipment and sampling ports, FI: flow measurement, GA: gas analysis, SP: sampling port. Adapted from ref 24. Available under CC-BY 4.0.

Experimental measurements are taken at various locations in the system. Eight thermocouples and 11 pressure measurements are installed over the height of the FR. Volume flow and gas composition are measured in the syngas line after the cyclone. From both loop seals, solid samples can be taken in batch intervals.

The pilot plant was operated with three different biogenic feedstocks: industrial wood pellets (IWP), pine forest residue (PFR), and wheat straw pellets (WSP). IWP is commercially available wood pellets conforming to the norm EN plus A1. PFR and WSP were produced from Swedish forestry residues and Swedish wheat straw, respectively, specifically for use in pilot operations. Norwegian ilmenite was used as an OC. A detailed description of the experiments in the pilot plant can be found elsewhere.[9,25]

Governing Equations. A standalone simulation of the FR was performed in ANSYS-FLUENT 21R2, using the Euler–Lagrange DEM. The DEM approach gives accurate results at the cost of a high computational effort due to the tracking of individual particles through the domain and the resolution of particle collisions.

According to the Euler–Lagrange approach, the gas phase is solved in the Eulerian frame of reference based on the Navier–Stokes equations, while the particles are treated as a discrete phase in the Lagrangian frame solving Newton's equation of motion. The governing equations are the conservation of mass, momentum, energy, and species. The conservation of mass equation is formulated as follows:

$$\frac{\partial(\varepsilon_g \rho_g)}{\partial t} + \nabla\cdot(\varepsilon_g \rho_g \vec{u}_g) = S^m_{p\to g} \tag{1}$$

The source term on the right side of the equation considers the mass transfer between the particles and the gas phase. The momentum equation can be written as

$$\frac{\partial(\varepsilon_g \rho_g \vec{u}_g)}{\partial t} + \nabla\cdot(\varepsilon_g \rho_g \vec{u}_g \vec{u}_g) = \nabla\cdot(\varepsilon_g \tau_f) - \varepsilon_g \nabla p + \varepsilon_g \rho_g \vec{g} + \vec{S}^u_{p\to f} \tag{2}$$

The source term $\vec{S}^u_{p\to g}$ describes the forces between the solid and the gas phases. τ_g is the fluid stress tensor, which is defined using the unit matrix I as

$$\tau_g = \varepsilon_g \mu_g \left[\left(\nabla \vec{u}_g + \nabla \vec{u}_g^{\,T}\right) - \frac{2}{3}\nabla\cdot\vec{u}_g I\right] \tag{3}$$

The energy conservation is calculated as follows:

$$\frac{\partial(\varepsilon_g \rho_g h)}{\partial t} + \nabla\cdot(\varepsilon_g \rho_g \vec{u}_g h_g) = \varepsilon_g \frac{\partial \rho_g}{\partial t} + \nabla\cdot\left(\frac{\varepsilon_g \mu_g}{Pr}\nabla h_g\right) + S^{reaction}_g + S^h_{p\to g} \tag{4}$$

This equation has two source terms: $S^{reaction}_g$ is the change in energy due to chemical reactions in the gas phase, while $S^h_{p\to g}$ is the energy transferred between gas and particle phases. Pr is

https://doi.org/10.1021/acs.energyfuels.4c02571
Energy Fuels 2024, 38, 18660–18673

the Prandtl number. Energy transferred by radiation is small due to the small temperature gradient over the reactor. Therefore, the effect of radiative heat transfer on the results is small while considerably increasing the computational effort. Thus, radiation was neglected in the model. The convective heat transfer between particles and gas phase is calculated according to the Ranz–Marshall model,[26,27] which is widely employed in the literature for fluidized bed simulations.[28] The formulation using the Nusselt number Nu, the heat transfer coefficient h, and the thermal conductivity of the gas phase k is written as follows:

$$Nu = \frac{hd_p}{k} = 2.0 + 0.6Re_d^{1/2}Pr^{1/3} \tag{5}$$

The species conservation is calculated for each species in the gas phase according to the following equation:

$$\frac{\partial(\varepsilon_g\rho_g y_i)}{\partial t} + \nabla\cdot(\varepsilon_g\rho_g\vec{u}_g y_i) = \nabla\cdot\left(\frac{\varepsilon_g\mu_g}{Sc}\nabla y_i\right) + S_g^y + S_{p\to g}^y \tag{6}$$

The source terms S_g^y and $S_{p\to g}^y$ describe the change in species fractions due to homogeneous and heterogeneous reactions, respectively. Sc is the Schmidt number.

The particle trajectories are calculated by solving Newton's equation of motion.

$$\rho_p\frac{d\vec{u}_p}{dt} = \Sigma\vec{F}_p = \vec{F}_{vol} + \vec{F}_{drag} + \vec{F}_{con} \tag{7}$$

The forces considered in this work are the gravitational and buoyancy forces $\vec{F}_{vol}$, drag force $\vec{F}_{drag}$, and contact forces $\vec{F}_{con}$.

$$\vec{F}_{vol} = \vec{g}(\rho_p - \rho_g) \tag{8}$$

For the calculation of the contact forces, the DEM uses the so-called soft sphere approach, schematically depicted in Figure 3. When particles collide with each other or the wall,

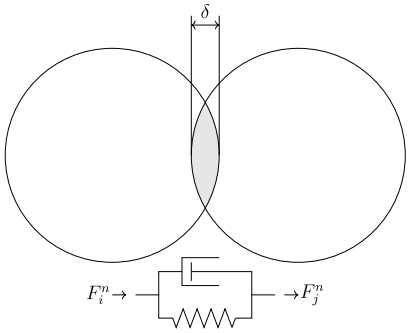

Figure 3. Schematic representation of a collision between two particles.

they are allowed to overlap each other. From the penetration depth, a restitution force is calculated using the spring–dashpot law, which models a parallel setup of a spring with a spring constant k and a damper element with a damping coefficient η. The spring models the ideal elastic collision, while the damping element corresponds to the energy dissipation in an inelastic collision. The normal contact force can thus be calculated as

$$\vec{F}_{con}^n = -K(\delta) - \eta\vec{u}_{ij} \tag{9}$$

The tangential collision forces are calculated based on Coulomb's friction as

$$\vec{F}_{con}^t = \mu\vec{F}_{con}^n \tag{10}$$

The linear spring–dashpot model was chosen, as it allows for larger particle time steps and therefore requires a lower computational effort.

Coarse Graining. Due to the large scale of the system and high solid loading, the tracking of all particles is computationally unfeasible. Therefore, the coarse-grained approach was used, in which several real particles are lumped together in an equivalent numerical particle, the so-called parcel. The parcel inherits the material properties from those of the real particle. The ratio R and scaling factor l between parcel and particle volumes is defined as follows:

$$R = \frac{V_{parcel}}{V_{particle}} = \left(\frac{d_{parcel}}{d_{particle}}\right)^3 = l^3 \tag{11}$$

The scaling factors used in this work can be found in Table 9. The particles are lumped into parcels so that each parcel contains only particles with identical properties. To divide the particles into parcels, several options are available. Most commonly, the same size or same statistic weight method is used. The same size method results in parcels with a uniform diameter. The same statistic weight method keeps a statistical particle property constant for all parcels, typically the number of particles. The same size method was chosen because it allows for a larger particle time step and thus faster simulation times. Particle collisions are calculated by using parcel mass and diameter. Source terms for heat and mass transfer are calculated at the particle level and scaled up to the parcel level. This leads to uniform parcel properties without gradients between particles.

Drag Model. The momentum exchange coefficient between the gas–solid phases interacting within the studied reactors is calculated based on the subgrid energy-minimization multiscale (EMMS) scheme. In contrast to the conventional Gidaspow model,[29] which considers almost homogeneous conditions in each computational cell, the EMMS model takes into account the mesoscale structural effect (clusters) on the calculation of the gas–solid drag coefficient in each computational cell,[16] through a dimensionless factor, the heterogeneity index, H_d. This model, initially proposed by Li and Kwauk,[30] has gained attention in the past decade by several research groups.[31] The version of the EMMS scheme that is used in this study is based on a previous work of CERTH proposed and validated by Zeneli et al.[32] for the case of a CFB carbonator and later on applied for the simulation of a variety of similar reactors.[32,33] The set of equations comprising the EMMS scheme is solved for any control volume. Solving this nonlinear optimization problem is not trivial and requires considerable CPU time if it is done in parallel with the solution of the transient 3D multiphase problem. Thus, a common technique applied for such calculations is to precalculate the solution of the EMMS system equations for any combination of input parameters. In the proposed formulation, only the local volume fraction and the fraction of slip velocity are considered as input parameters, whereas in the solution of the EMMS model, the gas–solid physical parameters are also taken into account (Table 1). The set of analytical, empirical, and semiempirical

https://doi.org/10.1021/acs.energyfuels.4c02571
Energy Fuels 2024, 38, 18660–18673

equations that constitute the present EMMS model can be found in ref 34.

Table 1. EMMS Model Parameters

reactor diameter D_r [m]	0.4
particle diameter d_p [μ m]	225
gas density ρ_g [kg m^{-3}]	0.13
solid density ρ_p [kg m^{-3}]	3710
gas viscosity μg [kg m^{-1}s^{-1}]	3.9×10^{-5}

This set of equations is solved through a custom-built code for discrete values of the gas, which is solved through u_{slip} (0.5, 1, 2, 3, 4, and 5) and the gas volume fraction ε_g within the range of ε_{mf} (0.55) to ε_{max}. This code calculates the drag force and consequently the heterogeneity index, for every combination of these two properties, by the following formula:

$$H_d(\varepsilon_g,\ u_{slip}) = \frac{F_{Wen\&Yu}}{F_{EMMS}} \tag{12}$$

where $F_{Wen\&Yu}$ is the drag force calculated by the model of Wen and Yu[35] and F_{EMMS} is the drag force calculated by the solution of the EMMS model as

$$F_{EMMS} = \varepsilon_g(\rho_p - \rho_g)[f(1-\varepsilon_c)(c+a_c) + (1-f)(1-\varepsilon_f)(g+a_f)] \tag{13}$$

The calculated H_d index is then interpolated using polynomials for three areas of ε_g: (i) area C: ε_g = [0.60, 0.82], (ii) area B: ε_g = [0.82, 0.95], and (iii) area A: ε_g = [0.96, ε_{max}]. As a last step, the resulting polynomials (Figure 4) are incorporated into the CFD model through a user-defined function (UDF) with the following general form:

$$H_d = a_6\varepsilon_g^6 + a_5\varepsilon_g^5 + a_4\varepsilon_g^4 + a_3\varepsilon_g^3 + a_2\varepsilon_g^2 + a_1\varepsilon_g + a_0 \tag{14}$$

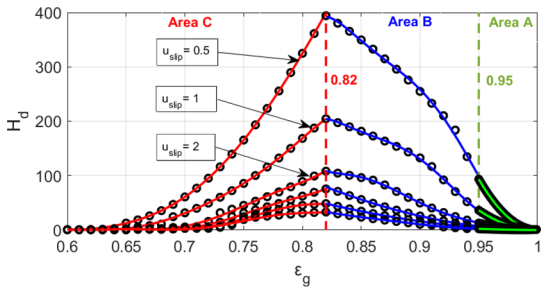

Figure 4. H_d index for different values of ε_g and u_{slip}.

Chemical Reactions. The chemistry in the FR was modeled with a simplified approach. In the gas phase, seven species, four species for the OC and three species for the biomass, were considered as shown in Table 2. The reactions can be categorized as OC reactions, heterogeneous fuel reactions, and homogeneous gas phase reactions. In each category, three reactions were considered.

$$\text{Biomass} \rightarrow C_{fix} + \text{Ash} + H_2 + CO + CO_2 + H_2O + CH_4 + \text{Tar} \tag{R1}$$

$$C + H_2O \rightarrow CO + H_2 \tag{R2}$$

Table 2. Chemical Species Used in the Model

gas phase	ilmenite	biomass
H_2	$FeTiO_3$	char
CO	TiO_2	volatiles
CO_2	Fe_2O_3	ash
CH_4	inert material	
tar		
H_2O		
N_2		

$$C + CO_2 \rightarrow 2CO \tag{R3}$$

The biomass first undergoes drying and pyrolysis. Both processes were modeled in a single step with a constant rate approach according to reaction R1. The species fractions of the volatile species had been determined by Di Giuliano et al.[36] for PFR and WSP. Since experimental data were not available for IWP, the PFR data were used, as both feedstocks are made up of woody biomasses. All hydrocarbon species larger than methane were lumped together as a single tar species. Experimental analysis by Di Giuliano et al.[36] identified the overall composition of the tars as approximately C_3H_8. Species fractions were fitted to the reactor temperature as shown in Table 3.

Table 3. Pyrolysis Gas Composition at the Reactor Temperature

species [vol %]	IWP	PFR	WSP
H_2	22	23	21
CO	41	41	38
CO_2	13	13	16
CH_4	16	16	16
tar	8	8	10

Gasification of fixed carbon was considered for steam and CO_2 as formulated in reactions R2 and R3. Kinetics were determined for all feedstocks used in this study by Abad et al.[37] The reaction rates were modeled with a Langmuir–Hinshelwood kinetic model, and the individual rate constants were determined through an Arrhenius equation:

$$\frac{dX_C}{dt}(1 - X_C) = \frac{k_r p_{gasif}}{1 + k_{gasif}p_{gasif} + k_{prod}p_{prod}} \tag{15}$$

$$k = k_0 \exp\left(\frac{-E_A}{RT}\right) \tag{16}$$

In this equation, p_{gasif} and p_{prod} are the partial pressures of the gasification medium and product, respectively. The kinetic data for the different feedstocks are shown in Table 4.

Ilmenite was modeled as Fe_2O_3, TiO_2, and $FeTiO_3$. In the oxidized state, the particle consists of Fe_2O_3 and TiO_2, which are converted to $FeTiO_3$ during reduction. This is a simplification of several parallel and competing reactions and species taking place in the particle to allow for simple one-step reduction kinetics. The reactions with hydrogen, carbon monoxide, and methane were considered as shown in reactions R4–R6. Due to the lower species fractions and reactivity, tar species as reduction agents were not considered.

$$Fe_2O_3 + 2TiO_2 + H_2 \rightarrow 2FeTiO_3 + H_2O \tag{R4}$$

https://doi.org/10.1021/acs.energyfuels.4c02571
Energy Fuels 2024, 38, 18660–18673

Table 4. Kinetic Parameters for Gasification Reactions[37]

	IWP		PFR		WSP	
kinetic parameters	H_2O	CO_2	H_2O	CO_2	H_2O	CO_2
$k_{r,0}$ [Pa^{-1} s^{-1}]	1.68×10^{-4}	5.72×10^{-4}	6.81×10^{-4}	1.38×10^{-3}	4.87×10^{-3}	4.7×10^{-4}
$E_{A,r}$ [kJ $kmol^{-1}$]	7.58×10^{4}	9.17×10^{4}	$8{,}99 \times 10^{4}$	1.01×10^{5}	1.08×10^{5}	8.49×10^{4}
$k_{gasif,0}$ [Pa^{-1}]	8.39×10^{-8}	7.5×10^{-9}	3.06×10^{-7}	2.66×10^{-8}	9.29×10^{-8}	1.36×10^{-9}
$E_{A,gasif}$ [kJ $kmol^{-1}$]	-5.53×10^{4}	-7.7×10^{4}	-4.14×10^{4}	-6.41×10^{4}	-5.31×10^{4}	-9.42×10^{4}
$k_{prod,0}$ [Pa^{-1}]	1.88×10^{-12}	9.87×10^{-11}	2.07×10^{-11}	3.06×10^{-12}	2.24×10^{-10}	7.04×10^{-12}
$E_{A,prod}$ [kJ $kmol^{-1}$]	-1.74×10^{5}	-1.31×10^{5}	-1.44×10^{5}	-1.62×10^{5}	-1.27×10^{2}	-1.55×10^{5}
n [−]	0.4		0		1	

$$Fe_2O_3 + 2TiO_2 + CO \rightarrow 2FeTiO_3 + CO2 \quad \text{(R5)}$$

$$4Fe_2O_3 + 8TiO_2 + CH_4 \rightarrow 8FeTiO_3 + CO_2 + 2H_2O \quad \text{(R6)}$$

The kinetics were determined by Abad et al. as shown in eqs 17 and 18.[38] The kinetic parameters for the OC reactions can be found in Table 5.

$$\frac{t}{\tau_{chr}} = 1 - (1 - X_{OC})^{1/3} \quad (17)$$

$$\tau_{chr} = \frac{\rho_m r_g}{\overline{b} k_s C_g^n} \quad (18)$$

Table 5. Kinetic Parameters for Ilmenite Reduction Reactions[38]

kinetic parameters	H_2	CO	CH_4
ρ_m [mol m^{-3}]	13,590	13,590	13,590
r_g [m]	1.25×10^{-6}	1.25×10^{-6}	1.25×10^{-6}
$\overline{b}$ [−]	1.45	1.45	5.78
k_{s0} [mol^{1-n} m^{3n-2} s^{-1}]	6.2×10^{-2}	1.0×10^{-1}	9.8
$E_{A,chr}$ [kJ mol^{-1}]	65.0	80.7	135.2
n [−]	1	0.8	1

τ_{chr} is the time until complete conversion of the particle, and t is the time until current conversion X_{OC} is reached.

In the gas phase, two main reactions occur, namely, the water gas shift reaction and the steam reforming of tars. Cracking of tars was neglected due to the low temperatures in the reactor. The water gas shift and reverse water gas shift reactions were implemented according to Klimanek et al.[39] The tar reforming kinetics shown in Table 6 were determined

Table 6. Kinetic Parameters for Homogeneous Gas Phase Reactions[39,40]

	k	E_A		
reaction	[$kmol^{1-n}$ $m^{-3(1-n)}$ s^{-1}]	[kJ $kmol^{-1}$]	n_1	n_2
R7	2.75×10^{6}	83,597	1	0.5
R8	1.04×10^{8}	116,479	0.5	1
	[m^3 kg^{-1} s^{-1}]	[kJ $kmol^{-1}$]		
R9	5.29×1.47^2	72,600	1	0

by Min et al.[40] for biomass tar in a fluidized bed with ilmenite as the bed material, thus accounting for catalytic effects of the OC.

$$CO + H_2O \rightarrow CO_2 + H_2 \quad \text{(R7)}$$

$$CO_2 + H_2 \rightarrow CO + H_2O \quad \text{(R8)}$$

$$Tar + 3H_2O \rightarrow 7H_2 + 3CO \quad \text{(R9)}$$

Boundary and Initial Conditions. In this work, the FR was simulated in a standalone configuration. Thus, only the riser and the connection to the cyclone were modeled as shown in Figure 5. The geometry was created and meshed

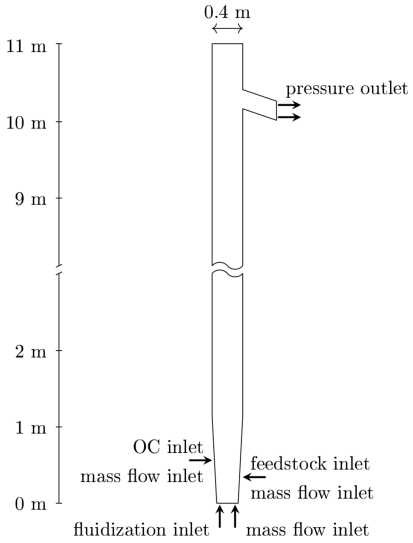

Figure 5. Computational domain of the FR.

using ANSYS-Design Modeler and ANSYS Meshing version 21R2, respectively. To achieve a structured mesh with uniform mesh size, the circular inlets along the side of the reactor were replaced by rectangular inlets with the same area in order to keep flow velocities constant. A hexahedral mesh with approximately 100,000 cells was created. Due to the limitations of the DEM approach, all cells need to be sufficiently larger than the largest parcel in the simulation. As the size of the parcels inversely correlates with the number of parcels, which in turn correlates with the computational effort, a further refinement of the mesh was unfeasible due to computational limitations. Therefore, a mesh independence study was not conducted. However, in simulations of a similar-sized reactor, 100,000 cells were found sufficient to achieve grid-independent results.[41]

For all three feedstocks, experimental data from stable operation in the 1 MW_{th} CLG unit at TU Darmstadt are available. Details about the plant operation were published by Marx et al.[9,24] and Dieringer et al.[25,42] The feedstock properties are listed in Table 7. For each feedstock, one long-term stable balance point was chosen for the simulation. Experimental measurements were averaged over 20 min to avoid effects from stochastic fluctuations. Table 8 shows the boundary conditions

https://doi.org/10.1021/acs.energyfuels.4c02571
Energy Fuels 2024, 38, 18660−18673

Table 7. Proximate and Ultimate Analysis of Feedstock Used during Experiments[a]

	component	IWP	PFR	WSP
PA [wt %]	moisture	8.3	4.4	10.8
	ash (dry base (d.b.))	0.3	2.3	4.7
	volatiles (d.b.)	84.6	80.3	77.0
	fixed carbon (d.b.)	15.1	17.4	18.3
UA [wt %]	C (d.b.)	50.7	51.1	50.0
	H (d.b.)	6.1	6.1	6.0
	N (d.b.)	0.33	0.44	0.56
	O (d.b.)	42.5	40.1	43.2
	S (d.b.)	0.008	0.025	0.11
	Cl (d.b.)	0.008	0.010	0.08
LHV [MJ kg^{-1}]		17.2	18.3	15.3

[a]LHV: lower heating value; PA: proximate analysis; UA: ultimate analysis; d.b.: dry base; IWP: industrial wood pellets; PFR: pine forest residue; WSP: wheat straw pellets.

Table 8. Experimental Data Are Used as Boundary Conditions

	IWP	PFR	WSP
OC circulation [kg/h]	8889	13,446	6478
OC inlet temperature [°C]	567	648	642
OC oxidation degree [%]	93.4	96.4	97.8
reactor inventory [kg]	84	65	61
fuel flow rate [kg/h]	223	301	352.5
steam flow rate [kg/h]	465	280	448
CO_2 flow rate [kg/h]	0	59	56
steam inlet temperature [°C]	375	464	448
LS fluidization [kg/h]	37	31	34

derived from the experimental data. The fluidization gas is prescribed as a uniform flow over the fluidization inlet boundary surface, which is an idealization of the nozzle bottom installed in the pilot plant. The fluidizing gas from the loop seal (LS) is assumed to follow the solid flow into the AR, while the gas from the J-Valve flows to the FR and is thus added through the OC inlet boundary surface. At the start of the simulation, the reactor is initialized with nitrogen to improve the numerical stability of the simulation by limiting the initial reaction rates.

The solids are initialized with a random distribution of both OC and partially gasified biomass char in the lower half of the reactor according to the experimentally determined inventory. Oxidization degree and PSD of the OC were interpolated from solid samples taken from both loop seals as shown in Tables 8 and 9. During the simulation time, the OC particles were fed to the reactor through the OC inlet. In CFD simulations of CFB reactors, the inventory is typically considered a fixed value, while the solid circulation is a free value.[41,43,44] For the CLG process, both oxygen transfer and heat transfer from the AR to the FR are directly related to the circulation. Thus, a correct particle influx to the FR is crucial for a good representation of the reactor thermodynamics. Therefore, in this work, particle circulation from the AR to the FR as a key parameter of the CLG process was selected as the fixed boundary condition, while the inventory was variable.

The fresh biomass from the screw feeder entered the reactor along the feedstock inlet boundary. In reality, pellets are fed to the reactor and disintegrate through devolatilization and abrasion. Due to the complex nature of this process, particle breakup was not modeled. Instead, the particle size of the fresh biomass was defined so that it reached 1 mm diameter after devolatilization, which was determined experimentally from LS samples. The walls of the reactor were modeled as no-slip walls. Particles can exit the reactor only at the outlet and are reflected at the inlet faces. Over the wall of the reactor, heat losses were considered using a constant stream of 5.5 kW/m^2 evenly distributed over the entire reactor wall. Turbulence of the gas flow was considered using the k-ε model with standard coefficients. Further numerical parameters can be found in Table 10.

Table 10. Numerical Settings of the Simulations

parameter	IWP	PFR	WSP
restitution coefficient k [N/m]	70	75	70
damping coefficient η	0.2	0.15	0.15
fluid time step [ms]	0.25	0.25	0.25
particle time step [ms]	0.02	0.02	0.02
turbulence	k-ε	k-ε	k-ε

Key Parameters. To evaluate the simulation results, two key parameters are introduced. The oxidation degree X_{OC} determines the fraction of OC that has been oxidized and thus is a measure of the oxygen stored in the OC. The amount of oxygen transferred from the AR to the FR can be determined from the oxidation degree of the OC in both loop seals. The oxidation degree is calculated from the current particle mass m_{OC}, the particle mass after full oxidation $m_{OC,ox}$, and the OC transport capacity R_{tr}.

$$X_{OC} = 1 - \frac{m_{OC,ox} - m_{OC}}{R_{tr} \cdot m_{OC,ox}} \tag{19}$$

The second key parameter is carbon conversion X_C. It shows the fraction of carbon in the feedstock which reacted into gaseous products.

Table 9. Initial PSD and Coarse Graining Factors of Ilmenite

IWP			PFR			WSP		
d_p [μm]	mass [wt %]	l	d_p [μm]	mass [wt %]	l	d_p [μm]	mass [wt %]	l
32.5	1.7	262	84.5	8.34	101	76.1	6.2	112
51.5	3.6	165	128	9.5	66	128	13.5	66
76.5	8.4	111	165	22.2	52	165	13.4	52
107.5	15.4	79	190	19.2	45	190	10.8	45
137.5	18.0	62	225	32.3	38	225	21.6	38
175	28.6	49	275	7.2	31	275	12.3	31
225	17.0	38	327.5	1.2	26	344	8.6	25
305	7.2	28	355	0.1	24	425	13.7	20

https://doi.org/10.1021/acs.energyfuels.4c02571
Energy Fuels 2024, 38, 18660−18673

$$X_C = \frac{\dot{n}_{syngas} \cdot (y_{CH_4} + y_{CO_2} + y_{CO} + m y_{C_mH_n}) \cdot \tilde{M}_C - \dot{m}_{fluidization} \cdot \frac{\tilde{M}_C}{\tilde{M}_{CO_2}}}{\dot{m}_{FS} \cdot x_{C,FS}} \quad (20)$$

Here, $\dot{n}_{syngas}$ is the molar gas flow rate at the reactor outlet, y_i the molar fractions of species i, and $\tilde{M}_C$ and $\tilde{M}_{CO_2}$ the molar mass of carbon and carbon dioxide. $\dot{m}_{fluidization}$ and $\dot{m}_{FS}$ are the mass flow rates of CO_2 at the reactor inlet and feedstock, respectively, and $x_{C,FS}$ is the mass fraction of C in the feedstock.

RESULTS AND DISCUSSION

Operation with the three different feedstocks IWP, PFR, and WSP was simulated and validated by experimental data. The simulations were conducted until a quasi-steady state with only small fluctuations of less than 5% around steady mean values was reached. The total simulation time varied from case to case, depending on how well the initial conditions represented the steady state. Typically, a steady state was reached after 10−20 s of simulated time. After the steady state was reached, simulations were continued for another 10 s over which the results were averaged.

In this section, the results are examined regarding the representation of the reactor hydrodynamics and thermodynamics in comparison to the experimental data. Details about the experimental measurements have been provided elsewhere and thus are omitted here.[9,24,25,45]

Hydrodynamics. The reactor hydrodynamics were evaluated based on the pressure profile over the height of the reactor and the reactor inventory. In Figure 6, the pressure profile over the reactor height is shown for all of the cases. The simulated profiles are in good agreement with the experimental measurements for all cases, especially with IWP. This indicates a correct representation of solid distribution throughout the reactor. For the PFR and WSP cases, a slight underprediction of the pressure drop over the dense bed at the bottom of the reactor can be observed. This can also be seen in the discrepancies in the reactor inventory shown in Table 11. For IWP, the inventory is predicted well, whereas it is underpredicted in the PFR and WSP cases. This is most likely due to a misrepresentation of the reactor PSD in the simulations, which has a significant impact on the reactor hydrodynamics.[25]

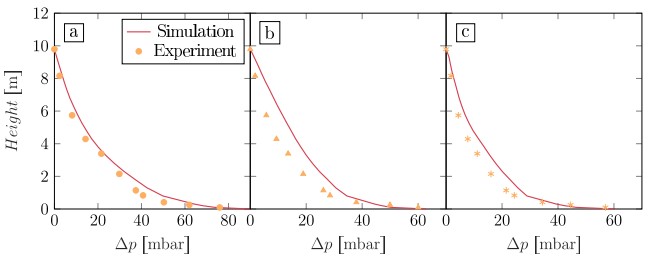

Figure 6. Simulated and experimental pressure profile over the height of the reactor. Feedstocks: (a) IWP, (b) PFR, and (c) WSP.

Table 11. Comparison of the Simulation and Experimental Reactor Inventories

	IWP	PFR	WSP
simulation	79.4	50.6	46.7
experiment	82.7	65.4	62.0

Due to very limited samples taken directly from the reactor bed, the PSD implemented in the simulations was taken from the loop seal samples. Small particles are entrained preferentially, as the surface-to-mass ratio is higher. Thus, the PSD of the loop seals has a higher fraction of fines than the reactor.[45] During the simulation, this first leads to a dip in the inventory as the fines escape the reactor, followed by a slow build-up and coarsening of the inventory. This difference in the PSD between the start and end of the simulation is shown to be exemplary for the IWP case in Figure 7. For the PFR and WSP cases, the bed material is coarser than that for IWP, leading to a larger discrepancy between the reactor and loop seal PSD and thus a longer simulation time until the steady state. Due to the available computational resources, the steady state could only be reached for IWP, leading to lower reactor inventories for PFR and WSP.

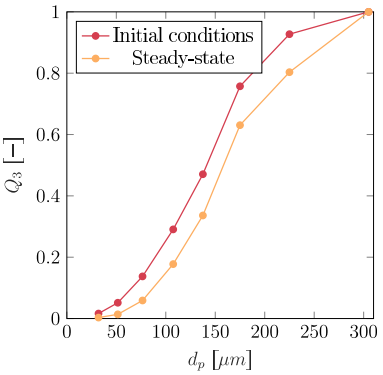

Figure 7. PSD in the reactor under initial conditions and the end of the simulation of IWP.

The particle velocity in the upward direction is depicted in Figure 8 for IWP. In the lower part of the reactor, a typical core-annulus flow with particles rising in the center and falling down along the walls can be observed. With increasing height, the gas flow through the outlet pulls the rising particles from the center toward the side of the reactor outlet. Thus, on the wall opposite the reactor outlet, the annulus becomes more pronounced with increasing reactor height. On the side of the outlet, the annulus becomes slower until it breaks down just below the outlet. At the outlet, only a fraction of the particles follow the gas stream to the cyclone, while the rest keep their upward trajectory due to inertia. Above the outlet, the particles move toward the opposite wall, where they fall down and form the annulus flow. The probability of a particle that reaches the top of the reactor to exit the cyclone is called entrainment probability. The values for all set points can be found in Table 12. The entrainment probability was analyzed experimentally in a scaled-down cold flow model of the 1 MW_{th} plant by Dieringer et al.[25] The values found in this study are in range with the cold flow model for the corresponding set points.

Thermodynamics. The thermodynamic evaluation is divided into three parts: solids conversion, syngas production, and reactor temperature.

Solids Conversion. In Figure 9, the OC oxidation degree and carbon conversion are compared between simulation and experiment. The ilmenite oxidation degree is determined experimentally as described by Marx et al.[9] by oxidation of samples taken at the loop seal behind the FR cyclone according to eq 19. The oxidation degree predicted by the model at the reactor outlet is in good agreement with the experimental data.

https://doi.org/10.1021/acs.energyfuels.4c02571
Energy Fuels 2024, 38, 18660−18673

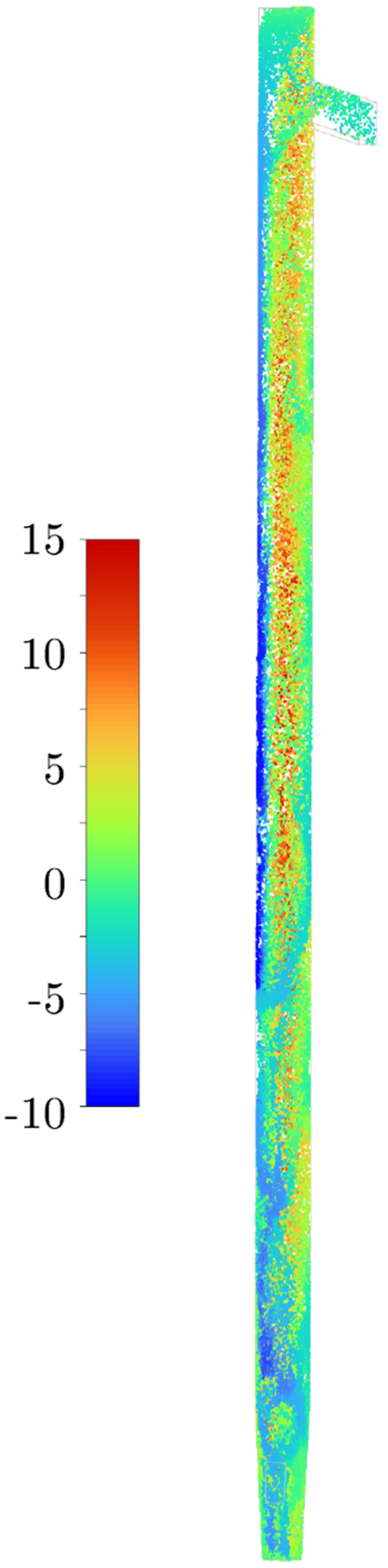

Figure 8. Particle velocity in the upward direction for IWP at the end of the simulation.

Table 12. Entrainment Probabilities for the Different Feedstocks

IWP	PFR	WSP
21.8	33.1	28.1

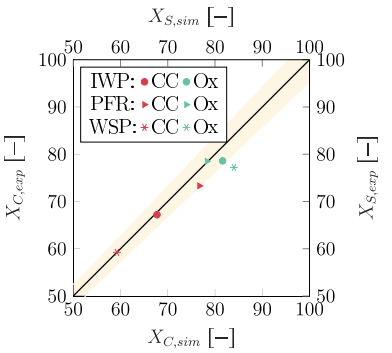

Figure 9. Carbon conversion and oxidation degree at the reactor outlet. The shaded area marks 5% deviation from the angle bisector.

Higher deviations for WSP can be attributed to uncertainties in the particle circulation measurements. Several parameters influence the OC conversion, most importantly the reaction kinetics and residence time. The implemented kinetics were specifically determined for ilmenite used in the experiments.[38] The simulation results confirm the validity of the kinetics and the applicability of the determination at the lab scale for large-scale plants. The agreement in the oxidation degree also indicates an accurate representation of OC residence times in the FR. The correct modeling of OC conversion is crucial for the gas composition, as it is directly linked to oxygen transfer to the FR and the closure of the heat balance.

Carbon conversion is evaluated according to eq 20 and shown in Figure 9. The simulation results accurately fit with the experimentally determined values. Carbon conversion depends on pyrolysis and subsequent gasification.

Carbon conversion through pyrolysis is mainly dependent on the particle temperature and heating rate. Heating curves for fuel particles determined from the simulations are depicted in Figure 10. The high reactor temperatures at the feeding position resulted in high heating rates that ranged from 771 K/s for IWP to 852 K/s for PFR. The simulation assumes feedstock as fragmented pellets of uniform temperature. Thermal conductivity inside the particles combined with larger diameters of the pellet likely leads to a lower heating rate.

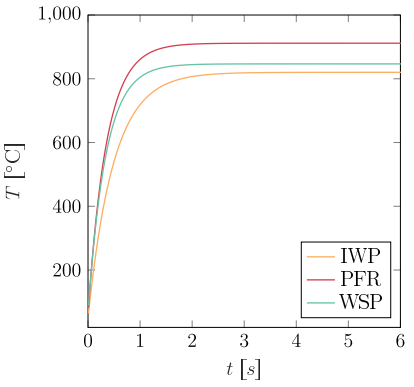

Figure 10. Heating of the feedstock particles.

https://doi.org/10.1021/acs.energyfuels.4c02571
Energy Fuels 2024, 38, 18660−18673

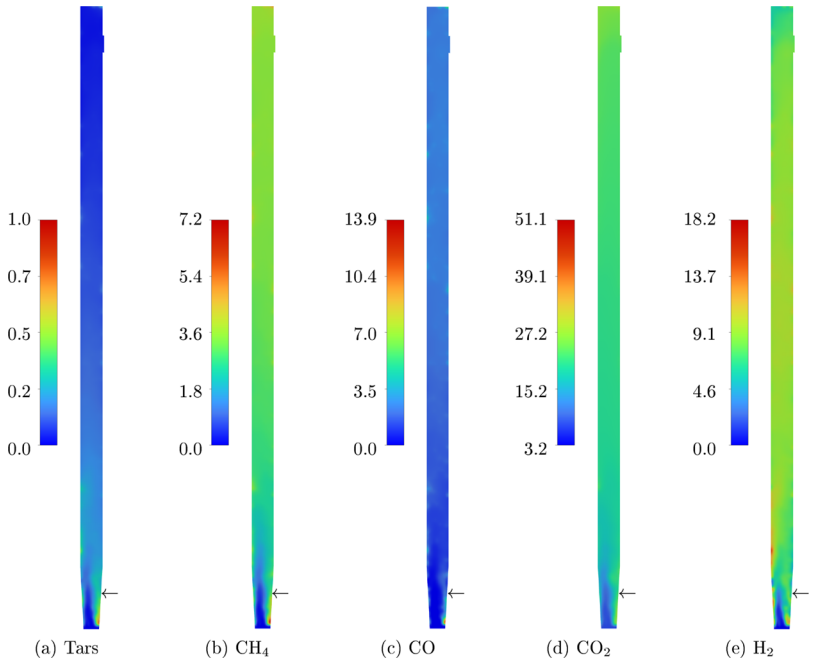

Figure 11. (a) Tars, (b) CH_4, (c) CO, (d) CO_2, and (e) H_2 instantaneous gas fractions in mol % for simulation with PFR after 25 s.

However, at reactor temperatures, the char conversion is mainly related to the final temperature with the heating rate having no significant influence.[55] The particle temperature reaches the reactor temperature after less than 2 s allowing for full conversion, which results in full conversion due to pyrolysis.

Carbon conversion due to gasification is comparatively slow. Therefore, the agreement between simulated and experimental carbon conversion indicates a correct modeling of gasification reactions and also highlights the validity of the kinetics for large-scale simulation.

Syngas Production. The gas species distribution over the reactor is shown for PFR in Figure 11. It is notable that the majority of the reactions happen in the bottom bed of the reactor. The influence of the feedstock feeding position can clearly be seen. A zone with a high fraction of volatile gases created by feedstock pyrolysis is established. With increasing height, the pyrolysis gases mix with the fluidizing media until the zones are completely mixed at around a quarter of the reactor height. Through subsequent gasification and tar decomposition reactions, the share of H_2 and CO increases slowly with increasing height, while the tar fraction decreases. No major trends are visible in the distribution of CH_4 due to the relatively slow oxidation kinetics with the OC.

The gas composition at the reactor outlet is shown and compared with experimental data in Figure 12. For IWP, higher fractions of H_2O and CO_2 and a lower fraction of H_2 and CO can be observed compared to PFR and WSP. This is caused by a higher air equivalence ratio of 0.23 for IWP compared to 0.14 and 0.15 for PFR and WSP, respectively. This leads to the oxidation of a larger fraction of H_2 and CO. PFR results show more H_2 and CO_2 in the product gas compared to WSP, while the CO and H_2O output is lower. This can be attributed to the water gas shift reaction which does not reach equilibrium in the reactor for both fuels.

The simulation results show good overall agreement with the experimental data. In particular, for CO_2, CH_4, and H_2O, the deviations are negligible. For H_2, the simulation over-

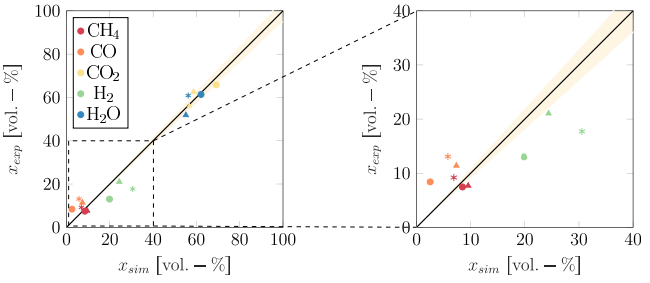

Figure 12. Gas composition on a dry basis and moisture at the reactor outlet. Feedstocks: ● IWP, ▶ PFR, and ★ WSP. The shaded area marks 10% deviation from the angle bisector.

predicts the production, while the CO fractions are somewhat underpredicted. Several simplifications were made during the simulation, which may affect the results. The computational domain extends only until the end of the riser and is cut off before the cyclone, where the gas composition is evaluated. In the experimental plant, the gas measurements are taken after the cyclone, which leads to longer residence times for the gas; therefore, gas compositions closer to the equilibrium of the water gas shift reaction at lower H_2 and higher CO fractions are expected. However, the water gas shift reaction is also affected by reactor temperatures, which is discussed below.

The composition of volatiles released during pyrolysis of the biomass pellets was modeled according to experimental data; however, there are some notable differences between the feedstocks in the pyrolysis experiments and the 1 MW_{th} pilot tests. For IWP, no pyrolysis data were available, so PFR data were used. For PFR and WSP, the biomass used in the pyrolysis tests was sourced from Spain, while the feedstock of the pilot tests was grown in Sweden. The composition of biomass depends on various conditions during growth, harvest, and storage periods.[46−49] Due to the different sources of the feedstocks, these parameters were not constant, so some deviation in the volatile composition is to be expected.

https://doi.org/10.1021/acs.energyfuels.4c02571
Energy Fuels 2024, 38, 18660−18673

Another reason may lie in the treatment of tars. Tars formed during pyrolysis of the feedstock are almost fully converted so that outlet concentrations between 0.7 and 7.1 g/m_N^3 are predicted. During the experiments, several tar measurements were taken; however, no measurement is available at the exact time period of the simulated balance points. Nevertheless, interpolation from other experimental balance points is possible. The values are higher than reported for the gravimetric tars that were found between 0.1 and 4.5 g/m_N^3 but lower than experimental values when accounting for C_2 and C_3 hydrocarbon species, which total to approximately 3 vol %.[24] The tar fraction released during pyrolysis was modeled according to the experimental data. However, these tars consist only of light tars as the condensable heavy tars are removed before measurements through an ice trap.[36] This leads to a lower amount of both light and heavy tars in the simulation, as light tars are formed during decomposition of heavy tars. Furthermore, the tar composition may also deviate from C_3H_8 as assumed in the simulations.

The product gas composition is also influenced by solid circulation. The simulations were set up according to microwave measurements behind the FR cyclone. Due to the design of the system, these measurements could only be calibrated in cold conditions and thus are not exact in hot environments. With higher OC circulation rates, more oxygen is transported to the FR, which leads to a higher conversion of H_2, CH_4, and CO. Comparison with offline analysis based on loop seal samples indicates that solid circulation might be underestimated by the microwave measurements for IWP and overestimated for PFR.[9]

Reactor Temperature. The temperature distribution over the reactor height is shown in Figure 13. While the simulated

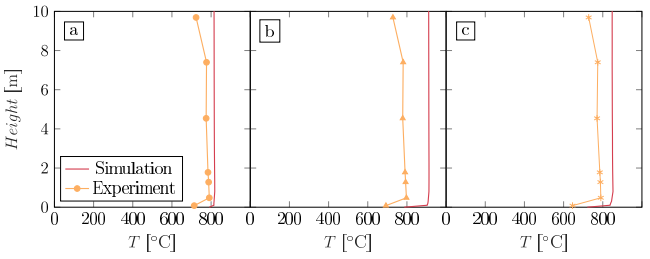

Figure 13. Temperature distribution over the reactor height. Feedstocks: (a) IWP, (b) PFR, and (c) WSP.

results correspond quite well to the experimental results for IWP operation, significant overprediction of the reactor temperature occurs in the PFR and WSP cases. This can be attributed to three main factors. In the simulation, pyrolysis reactions are assumed to be isothermal, and the heat of reaction for gasification is determined from standard state enthalpies considering char as pure carbon. This is a simplification, as the actual heat balance of both reactions depends on several factors during pyrolysis. For the heat of pyrolysis, both endo- and exothermic values have been reported, although the endothermic processes usually dominate at ambient pressure.[50] For the conditions present in this study, values between 200 kJ/kg and 1.6 MJ/kg were reported for wood[51,52] while for wheat straw, currently no values are available. An accurate estimation is difficult due to a variety of factors influencing the heat of pyrolysis.

A higher lignin content is associated with more exothermal behavior.[51,53] This could explain the lower temperature of IWP compared to WSP, which has a lower lignin content. In contrast, PFR, which has the highest lignin content, also has the highest overprediction of the temperature. However, PFR has the highest amount of fixed carbon, while also showing the highest carbon conversion of the feedstocks. Therefore, pyrolysis is less relevant, and the heat balance of the gasification reactions has a larger impact on reactor temperatures.

The char was modeled as pure carbon; therefore, a heat of formation of zero was assumed. In reality, for biomass chars, the enthalpy of formation is negative; therefore, the heat of gasification is more endothermal than modeled.[54] This also leads to an overestimation of reactor temperature and is particularly relevant in the cases with high carbon conversion such as PFR.

The solid circulation also influences the reactor temperature as the AR operates at higher temperatures, and the circulation is necessary for providing heat to the FR. The uncertainties in the solid circulation propagate into the reactor temperatures. This could add to the temperature overestimation for PFR, while it has the opposite effect on IWP.

Furthermore, heat losses over the reactor walls are not known precisely. The simulation uses uniform convective boundary conditions for the walls. In reality, due to the modular design of the pilot plant, a uniform boundary is not applicable. The stronger temperature gradient at the reactor top indicates an underprediction of heat losses in the simulation.

In summary, the model correctly predicts gasification reactions and ilmenite conversion, while the pyrolysis step leaves room for improvement. Although experimental data for the pyrolysis gas composition were available, discrepancies occurred due to the negligence of heavy tars. Further experiments with tar measurement equipment are necessary to improve the modeling of the release of pyrolysis gases. Alternatively, pyrolysis models based on comparatively simple fuel analysis are available in the literature.[55,56] However, the results of these models deviate significantly from experimental measurements, so experimental data are to be preferred if available. In addition, the heat of pyrolysis has a significant influence on the reactor and, thus, should not be neglected. While direct measurement is difficult, an estimation is possible when the pyrolysis gas composition is available. Finally, the kinetic rate of pyrolysis is not represented correctly by the constant rate approach. This most likely has only a minor influence on the outlet composition; however, in the region of the feedstock inlet port, it may be significant. Furthermore, accurate results require the correct implementation of the boundary conditions. Especially for OC circulation, this is a challenge, as an online measurement is difficult to implement and calibrate, and offline measurements also have high uncertainties, which may require an iterative approach.

CONCLUSIONS

A 3D CFD-DEM model for CLG using biomass as a feedstock was developed. Simulations of steady-state operation were conducted for three feedstocks: IWP, PFR, and WSP. Results were evaluated based on experimental data from the 1 MW_{th} pilot plant located at Darmstadt, Germany. The main findings can be concluded as follows:

1. The simulation showed good agreement with experimental data. In particular, the hydrodynamics and solids

https://doi.org/10.1021/acs.energyfuels.4c02571
Energy Fuels 2024, 38, 18660−18673

conversion show minor deviations. Pressure drop over the reactor is predicted with a mean error below 10%, and carbon and ilmenite conversion reach a mean error below 5%. For the gas composition, higher deviations were found for H_2 and CO with 8 and 6 mol % respectively.

2. DEM simulation of large-scale CLG units is possible in a reasonable time frame with appropriate simplifications. Using a simplified reaction model in combination with the coarse-grained approach, acceptable results can be achieved. This enables DEM as a tool for reactor design and scale-up while retaining information about processes on a particle scale.
3. The pyrolysis stage was identified as a crucial step for the accurate modeling of gas composition and reactor temperature. Both carbon conversion and volatile species vary with different pyrolysis conditions and significantly influence the products at the reactor outlet. Currently, no models are able to accurately predict this behavior; thus, an approach based on experimental data is suggested.

In future works, this model can be employed for optimization of operating conditions as well as reactor design for scale-up to the industrial scale.

AUTHOR INFORMATION

Corresponding Author

Christoph Graf − *Institute for Energy Systems and Technology, Department of Mechanical Engineering, Technical University Darmstadt, 64287 Darmstadt, Germany;* orcid.org/0009-0001-4435-1465; Phone: +49 6151 1622689; Email: christoph.graf@est.tu-darmstadt.de

Authors

Florian Coors − *Institute for Energy Systems and Technology, Department of Mechanical Engineering, Technical University Darmstadt, 64287 Darmstadt, Germany*

Falko Marx − *Institute for Energy Systems and Technology, Department of Mechanical Engineering, Technical University Darmstadt, 64287 Darmstadt, Germany*

Paul Dieringer − *Institute for Energy Systems and Technology, Department of Mechanical Engineering, Technical University Darmstadt, 64287 Darmstadt, Germany; A.H.T. Syngas Technology N.V., 51491 Overath, Germany;* orcid.org/0000-0003-4175-6800

Myrto Zeneli − *Centre for Research and Technology Hellas, Chemical Process and Energy Resources Institute (CERTH/CPERI), Athens Branch, Marousi, Athens GR-15125, Greece*

Panagiotis Stamatopoulos − *Centre for Research and Technology Hellas, Chemical Process and Energy Resources Institute (CERTH/CPERI), Athens Branch, Marousi, Athens GR-15125, Greece*

Konstantinos Atsonios − *Centre for Research and Technology Hellas, Chemical Process and Energy Resources Institute (CERTH/CPERI), Athens Branch, Marousi, Athens GR-15125, Greece;* orcid.org/0000-0002-5549-2650

Falah Alobaid − *Institute for Energy Systems and Technology, Department of Mechanical Engineering, Technical University Darmstadt, 64287 Darmstadt, Germany; Department of Energy Technology, Industrial Energy System, Lappeenranta-Lahti University of Technology (LUT), 53850 Lappeenranta, Finland*

Jochen Ströhle − *Institute for Energy Systems and Technology, Department of Mechanical Engineering, Technical University Darmstadt, 64287 Darmstadt, Germany*

Bernd Epple − *Institute for Energy Systems and Technology, Department of Mechanical Engineering, Technical University Darmstadt, 64287 Darmstadt, Germany*

Complete contact information is available at: https://pubs.acs.org/10.1021/acs.energyfuels.4c02571

Author Contributions

C.G.: conceptualization, methodology, software, validation, writing—original draft, writing—review and editing, visualization; F.C.: software, validation; F.M.: data curation, writing—review and editing; P.D.: data curation, writing—review and editing; M.Z.: methodology, writing—review and editing; P.S.: methodology, writing—review and editing, visualization; K.A.: writing—review and editing, supervision; F.A.: writing—review and editing, supervision; J.S.: writing—review and editing, project administration, funding acquisition; B.E.: supervision, funding acquisition.

Funding

This work has received funding from the European Union's Horizon 2020—Research and Innovation Framework Programme under grant agreement no. 817841 (Chemical Looping gAsification foR sustainAble production of biofuels—CLARA). The content of this work reflects only the author's view, and the European Commission is not responsible for any use that may be made of the information it contains.

Notes

The authors declare no competing financial interest.

ACKNOWLEDGMENTS

The authors gratefully acknowledge the computing time provided to them on the high-performance computer Lichtenberg at the NHR Centers NHR4CES at TU Darmstadt. This is funded by the Federal Ministry of Education and Research and the state governments participating on the basis of the resolutions of the GWK for national high-performance computing at universities.

ABBREVIATIONS

AR	air reactor
CFB	circulating fluidized bed
CFD	computational fluid dynamics
CLC	chemical looping combustion
CLG	chemical looping gasification
d.b.	dry base
DEM	discrete element method
EMMS	energy-minimization multiscale
FR	fuel reactor
IWP	industrial wood pellets
KTGF	kinetic theory of granular flows
LS	loop seal
MP-PIC	multiphase particle-in-cell
OC	oxygen carrier
PA	proximate analysis
PFR	pine forest residue
PSD	particle size distribution
TFM	two-fluid model
UA	ultimate analysis
UDF	user-defined function

WSP wheat straw pellets

SYMBOLS

C_g reacting gas concentration, mol m^{-3}
E_A activation energy, J mol^{-1}
K spring constant, N m^{-1}
LHV lower heating value, MJ kg^{-1}, MJ mol^{-1}
Pr Prandtl number
R_{tr} oxygen transport capacity
R universal gas constant, J mol^{-1} K^{-1}
Sc Schmidt number
S general source term
T temperature, K, °C
X conversion of reacting species
δ particle overlap, m
$\dot{m}$ mass flow, kg s^{-1}
$\dot{n}$ molar flow, mol s^{-1}
η damping coefficient
μ_g gas viscosity, kg m^{-1} s^{-1}
μ friction coefficient
$\overline{b}$ average stoichiometric coefficient for reaction of solid with reacting gas
ρ density, kg m^{-3}
τ_f fluid stress tensor
τ_{chr} time for complete conversion, s
M molar mass, atomic mass, g mol^{-1}
ε volume fraction
$\vec{F}$ force, N
$\vec{g}$ gravitational acceleration, m s^{-2}
d diameter, m
f dense phase volume fraction, $m^3_{dense\ phase}/m^3_{cell}$
h enthalpy, J kg^{-1}
n order of reaction
p pressure, Pa, bar
r_g grain radius, m
u velocity, m s^{-1}
x mass fraction in the solid phase
y mole fraction in the gas phase

Subscripts

OC oxygen carrier
con contact
gasif gasifying species
g gas phase
mf minimum fluidization
m molar
ox oxidized
prod product species
p particle
r reactor
vol volumetric

REFERENCES

(1) Lamb, W. F.; et al. A Review of Trends and Drivers of Greenhouse Gas Emissions by Sector from 1990 to 2018. *Environmental Research Letters* **2021**, *16*, No. 073005.

(2) Langner, E.; Kaltenmorgen, J.; Heinze, C.; Ströhle, J.; Epple, B. Fluidized Bed Gasification of Solid Recovered Fuels in a 500 kWth Pilot Plant. *Fuel* **2023**, *344*, No. 127901.

(3) Heinze, C.; May, J.; Langner, E.; Ströhle, J.; Epple, B. High Temperature Winkler Gasification of Rhenish Lignite in an Optimized 500 kWth Pilot Plant. *Fuel* **2023**, *333*, No. 126289.

(4) Hanel, A.; Dieterich, V.; Bastek, S.; Spliethoff, H.; Fendt, S. Entrained Flow Gasification-Based Biomass-to-X Processes: An Energetic and Technical Evaluation. *Energy Conversion and Management* **2022**, *274*, No. 116424.

(5) Dieringer, P.; Marx, F.; Alobaid, F.; Ströhle, J.; Epple, B. Process Control Strategies in Chemical Looping Gasification—A Novel Process for the Production of Biofuels Allowing for Net Negative CO2 Emissions. *Applied Sciences* **2020**, *10*, 4271.

(6) Condori, O.; García-Labiano, F.; Diego, L. F.; Izquierdo, M. T.; Abad, A.; Adánez, J. Biomass Chemical Looping Gasification for Syngas Production Using Ilmenite as Oxygen Carrier in a 1.5 kWth Unit. *Chem. Eng. J.* **2021**, *405*, No. 126679.

(7) Huseyin, S.; Wei, G.; Li, H.; He, F.; Huang, Z. Chemical-Looping Gasification of Biomass in a 10 kWth Interconnected Fluidized Bed Reactor Using Fe2O3/Al2O3 Oxygen Carrier. *J. Fuel Chem. Technol.* **2014**, *42*, 922−931.

(8) Ge, H.; Zhang, H.; Guo, W.; Song, T.; Shen, L. System Simulation and Experimental Verification: Biomass-based Integrated Gasification Combined Cycle (BIGCC) Coupling with Chemical Looping Gasification (CLG) for Power Generation. *Fuel* **2019**, *241*, 118−128.

(9) Marx, F.; Dieringer, P.; Ströhle, J.; Epple, B. Solid Flux Measurement in Dual Fluidized Bed Processes Based on Solid Samples. *Fuel* **2023**, *341*, No. 127589.

(10) Li, Z.; Xu, H.; Yang, W.; Xu, M.; Zhao, F. Numerical Investigation and Thermodynamic Analysis of Syngas Production through Chemical Looping Gasification Using Biomass as Fuel. *Fuel* **2019**, *246*, 466−475.

(11) Du, W.; Ma, L.; Pan, Q.; Dai, Q.; Zhang, M.; Yin, X.; Xiong, X.; Zhang, W. Full-Loop CFD Simulation of Lignite Chemical Looping Gasification with Phosphogypsum as Oxygen Carrier Using a Circulating Fluidized Bed. *Energy* **2023**, *262*, No. 125451.

(12) Zhang, Y.; Chao, Z.; Jakobsen, H. A. Modelling and Simulation of Chemical Looping Combustion Process in a Double Loop Circulating Fluidized Bed Reactor. *Chemical Engineering Journal* **2017**, *320*, 271−282.

(13) Mahalatkar, K.; Kuhlman, J.; Huckaby, E. D.; O'Brien, T. CFD Simulation of a Chemical-Looping Fuel Reactor Utilizing Solid Fuel. *Chem. Eng. Sci.* **2011**, *66*, 3617−3627.

(14) Alobaid, F.; Ohlemüller, P.; Ströhle, J.; Epple, B. Extended Euler−Euler Model for the Simulation of a 1 MWth Chemical−Looping Pilot Plant. *Energy* **2015**, *93*, 2395−2405.

(15) May, J.; Alobaid, F.; Ohlemüller, P.; Stroh, A.; Ströhle, J.; Epple, B. Reactive Two−Fluid Model for Chemical−Looping Combustion−Simulation of Fuel and Air Reactors. *International Journal of Greenhouse Gas Control* **2018**, *76*, 175−192.

(16) Yu, J.; Wang, S.; Kong, D.; Luo, K.; Fan, J. Coal-Fueled Chemical Looping Gasification: A CFD-DEM Study. *Fuel* **2023**, *345*, No. 128119.

(17) Lin, J.; Luo, K.; Wang, S.; Sun, L.; Fan, J. Particle-Scale Study of Coal-Direct Chemical Looping Combustion (CLC). *Energy* **2022**, *250*, No. 123859.

(18) Banerjee, S.; Agarwal, R. Transient Reacting Flow Simulation of Spouted Fluidized Bed for Coal-Direct Chemical Looping Combustion with Different Fe-based Oxygen Carriers. *Applied Energy* **2015**, *160*, 552−560.

(19) Luo, C.; Peng, Z.; Doroodchi, E.; Moghtaderi, B. A Three-Dimensional Hot Flow Model for Simulating the Alumina Encapsulated NI-NIO Methane-Air CLC System Based on the Computational Fluid Dynamics-Discrete Element Method. *Fuel* **2018**, *224*, 388−400.

(20) Dymala, T.; Wang, S.; Jarolin, K.; Song, T.; Shen, L.; Dosta, M.; Heinrich, S. MP-PIC Simulation of Biomass Steam Gasification Using Ilmenite as an Oxygen Carrier. *Atmosphere* **2022**, *13*, 1009.

(21) Reinking, Z.; Shim, H.-S.; Whitty, K. J.; Lighty, J. S. Computational Simulation of a 100 kW Dual Circulating Fluidized Bed Reactor Processing Coal by Chemical Looping with Oxygen Uncoupling. *International Journal of Greenhouse Gas Control* **2019**, *90*, No. 102795.

(22) Ahmed, I.; de Lasa, H. CO 2 Capture Using Chemical Looping Combustion from a Biomass-Derived Syngas Feedstock: Simulation

https://doi.org/10.1021/acs.energyfuels.4c02571
Energy Fuels 2024, 38, 18660−18673

of a Riser−Downer Scaled-Up Unit. *Ind. Eng. Chem. Res.* **2020**, *59*, 6900−6913.
(23) Marx, F.; Dieringer, P.; Ströhle, J.; Epple, B. Design of a 1 MWth Pilot Plant for Chemical Looping Gasification of Biogenic Residues. *Energies* **2021**, *14*, 2581.
(24) Marx, F.; Dieringer, P.; Ströhle, J.; Epple, B. Process Efficiency and Syngas Quality from Autothermal Operation of a 1 MWth Chemical Looping Gasifier with Biogenic Residues. *Applications in Energy and Combustion Science* **2023**, *16*, No. 100217.
(25) Dieringer, P.; Marx, F.; Ströhle, J.; Epple, B. System Hydrodynamics of a 1 MWth Dual Circulating Fluidized Bed Chemical Looping Gasifier. *Energies* **2023**, *16*, 5630.
(26) Ranz, W. E.; Marshall, W., Jr. Vaporation from Drops, Part I. *Chem. Eng. Prog.* **1952**, *48*, 141−146.
(27) Ranz, W. E.; Marshall, W., Jr. Evaporation from Drops, Part I and Part II. *Chem. Eng. Prog.* **1952**, *48*, 173−180.
(28) Alobaid, F.; Almohammed, N.; Massoudi Farid, M.; May, J.; Rößger, P.; Richter, A.; Epple, B. Progress in CFD Simulations of Fluidized Beds for Chemical and Energy Process Engineering. *Prog. Energy Combust. Sci.* **2022**, *91*, No. 100930.
(29) Gidaspow, D. *Multiphase Flow and Fluidization: Continuum and Kinetic Theory Descriptions*; Academic Press, 1994.
(30) Li, J.; Kwauk, M. Exploring Complex Systems in Chemical Engineering—the Multi-Scale Methodology. *Chem. Eng. Sci.* **2003**, *58*, 521−535.
(31) Wang, J.; Ge, W.; Li, J. Eulerian Simulation of Heterogeneous Gas−Solid Flows in CFB Risers: EMMS-based Sub-Grid Scale Model with a Revised Cluster Description. *Chem. Eng. Sci.* **2008**, *63*, 1553−1571.
(32) Zeneli, M.; Nikolopoulos, A.; Nikolopoulos, N.; Grammelis, P.; Karellas, S.; Kakaras, E.A Numericalstudy of the carbonator design effect on co2 capture efficiency. In *Conference: CFB-12At: Krakow, Poland*, 2018.
(33) Kanellis, G.; Zeneli, M.; Nikolopoulos, N.; Hofmann, C.; Ströhle, J.; Karellas, S.; Konttinen, J. CFD Modelling of an Indirectly Heated Calciner Reactor, Utilized for CO2 Capture, in an Eulerian Framework. *Fuel* **2023**, *346*, No. 128251.
(34) Zeneli, M.; Nikolopoulos, A.; Nikolopoulos, N.; Grammelis, P.; Kakaras, E. Application of an Advanced Coupled EMMS-TFM Model to a Pilot Scale CFB Carbonator". *Chemical Engineering Science, Bd* **2015**, *138*, 482−498.
(35) Wen, C. Y.; Yu, Y. H. A Generalized Method for Predicting the Minimum Fluidization Velocity". *AIChE J, Bd.* **1966**, *12*, 610−612.
(36) Di Giuliano, A.; Lucantonio, S.; Gallucci, K. Devolatilization of Residual Biomasses for Chemical Looping Gasification in Fluidized Beds Made Up of Oxygen-Carriers. *Energies* **2021**, *14*, 311.
(37) Abad, A.; Condori, O.; De Diego, L. F.; García-Labiano, F.; Adanez, J. Determination of the Intrinsic Kinetics of Biomass Gasification and Its Application to Resistant Pellets for Chemical Looping Gasification. *Fire* **2024**, *to be submitted* .
(38) Abad, A.; Adánez, J.; Cuadrat, A.; García-Labiano, F.; Gayán, P.; Diego, L. F. Kinetics of Redox Reactions of Ilmenite for Chemical-Looping Combustion. *Chem. Eng. Sci.* **2011**, *66*, 689−702.
(39) Klimanek, A.; Adamczyk, W.; Katelbach-Woźniak, A.; Wecel, G.; Szlek, A. Towards a Hybrid Eulerian−Lagrangian CFD Modeling of Coal Gasification in a Circulating Fluidized Bed Reactor. *Fuel* **2015**, *152*, 131−137.
(40) Min, Z.; Yimsiri, P.; Asadullah, M.; Zhang, S.; Li, C.-Z. Catalytic Reforming of Tar during Gasification. Part II. Char as a Catalyst or as a Catalyst Support for Tar Reforming. *Fuel* **2011**, *90*, 2545−2552.
(41) Nikolopoulos, A.; Stroh, A.; Zeneli, M.; Alobaid, F.; Nikolopoulos, N.; Ströhle, J.; Karellas, S.; Epple, B.; Grammelis, P. Numerical Investigation and Comparison of Coarse Grain CFD−DEM and TFM in the Case of a 1 MW Th Fluidized Bed Carbonator Simulation. *Chem. Eng. Sci.* **2017**, *163*, 189−205.
(42) Dieringer, P.; Marx, F.; Michel, B.; Ströhle, J.; Epple, B. Design and Control Concept of a 1 MWth Chemical Looping Gasifier Allowing for Efficient Autothermal Syngas Production. *International Journal of Greenhouse Gas Control* **2023**, *127*, No. 103929.
(43) Stroh, A.; Alobaid, F.; Bohnstein, M.; Ströhle, J.; Epple, B. Numerical CFD Simulation of 1 MWth Circulating Fluidized Bed Using the Coarse Grain Discrete Element Method with Homogenous Drag Models and Particle Size Distribution. *Fuel Process. Technol.* **2018**, *169*, 84−93.
(44) Zafiryadis, F.; Jensen, A. D.; Laxminarayan, Y.; Lin, W.; Hove, E. A.; Larsen, M. B.; Wu, H. Predicting Cold Gas-Solid Flow in a Pilot-Scale Dual-Circulating Fluidized Bed: Validation of Computational Particle Fluid Dynamics Model. *Powder Technol.* **2021**, *381*, 25−43.
(45) Dieringer, P.; Marx, F.; Lebendig, F.; Müller, M.; Di Giuliano, A.; Gallucci, K.; Ströhle, J.; Epple, B. Fate of Ilmenite as Oxygen Carrier during 1 MWth Chemical Looping Gasification of Biogenic Residues. *Applications in Energy and Combustion Science* **2023**, *16*, No. 100227.
(46) Surendra, K. C.; Ogoshi, R.; Zaleski, H. M.; Hashimoto, A. G.; Khanal, S. K. High Yielding Tropical Energy Crops for Bioenergy Production: Effects of Plant Components, Harvest Years and Locations on Biomass Composition. *Bioresource technology* **2018**, *251*, 218−229.
(47) Hodgson, E. M.; Lister, S. J.; Bridgwater, A. V.; Clifton-Brown, J.; Donnison, I. S. Genotypic and Environmentally Derived Variation in the Cell Wall Composition of Miscanthus in Relation to Its Use as a Biomass Feedstock. *Biomass and Bioenergy* **2010**, *34*, 652−660.
(48) Lewandowski, I.; Kicherer, A. Combustion Quality of Biomass: Practical Relevance and Experiments to Modify the Biomass Quality of Miscanthus x Giganteus. *European Journal of Agronomy* **1997**, *6*, 163−177.
(49) Meehan, P. G.; Finnan, J. M.; Mc Donnell, K. P. The Effect of Harvest Date and Harvest Method on the Combustion Characteristics of Miscanthus × Giganteus. *GCB Bioenergy* **2013**, *5*, 487−496.
(50) Di Blasi, C. Modeling Chemical and Physical Processes of Wood and Biomass Pyrolysis. *Prog. Energy Combust. Sci.* **2008**, *34*, 47−90.
(51) Rath, J.; Wolfinger, M. G.; Steiner, G.; Krammer, G.; Barontini, F. Heat of Wood Pyrolysis. *Fuel* **2003**, *82*, 81−91.
(52) Daugaard, D. E.; Brown, R. C. Enthalpy for Pyrolysis for Several Types of Biomass. *Energy Fuels* **2003**, *17*, 934−939.
(53) Chen, Q.; Yang, R.; Zhao, B.; Li, Y.; Wang, S.; Wu, H.; Zhuo, Y.; Chen, C. Investigation of Heat of Biomass Pyrolysis and Secondary Reactions by Simultaneous Thermogravimetry and Differential Scanning Calorimetry. *Fuel* **2014**, *134*, 467−476.
(54) Popescu, F.; Mahu, R.; Ion, I. V.; Rusu, E. A Mathematical Model of Biomass Combustion Physical and Chemical Processes. *Energies* **2020**, *13*, 6232.
(55) Neves, D.; Thunman, H.; Matos, A.; Tarelho, L.; Gómez-Barea, A. Characterization and Prediction of Biomass Pyrolysis Products. *Prog. Energy Combust. Sci.* **2011**, *37*, 611−630.
(56) Anca-Couce, A.; Sommersacher, P.; Scharler, R. Online Experiments and Modelling with a Detailed Reaction Scheme of Single Particle Biomass Pyrolysis. *Journal of Analytical and Applied Pyrolysis* **2017**, *127*, 411−425.

https://doi.org/10.1021/acs.energyfuels.4c02571
Energy Fuels 2024, 38, 18660−18673